


Trapped-Ion Quantum Computer with Robust Entangling Gates and Quantum Coherent Feedback

Tom Manovitz^{1,*,†,§}, Yotam Shapira^{1,†,§}, Lior Gazit, Nitzan Akerman, and Roei Ozeri
Department of Physics of Complex Systems and AMOS, Weizmann Institute of Science, Rehovot 7610001, Israel

 (Received 8 November 2021; accepted 24 February 2022; published 22 March 2022)

Quantum computers are expected to achieve a significant speed-up over classical computers in solving a range of computational problems. Chains of ions held in a linear Paul trap are a promising platform for constructing such quantum computers, due to their long coherence times and high quality of control. Here, we report on the construction of a small five-qubit universal quantum computer using $^{88}\text{Sr}^+$ ions in a radio-frequency (rf) trap. All basic operations, including initialization, quantum logic operations, and readout, are performed with high fidelity. Selective two-qubit and single-qubit gates, implemented using a narrow-line-width laser, comprise a universal gate set, allowing realization of any unitary on the quantum register. We review the main experimental tools and describe in detail unique aspects of the computer: the use of robust entangling gates and the development of a quantum coherent feedback system through electron-multiplying CCD camera acquisition. The latter is necessary for carrying out quantum error-correction protocols in future experiments.

DOI: [10.1103/PRXQuantum.3.010347](https://doi.org/10.1103/PRXQuantum.3.010347)

I. INTRODUCTION

Ion traps are among the leading quantum computing platforms explored today due to their strong isolation from the environment and naturally long coherence times. Trapped-ion quantum systems offer extremely accurate and reliable single-qubit and many-qubit operations; high-fidelity state preparation and measurement; and high connectivity between qubits, supported by the long-range Coulomb interaction between ions [1].

Several approaches are currently pursued in order to scale up trapped-ion quantum computing to a macroscopic number of qubits. These include shuttling of ions between different trapping regions in a CCD-like array of traps [2–4] and the heralded entanglement of ions in different traps using Hong-Ou-Mandel interference and detection of photons that are scattered by these ions [5,6]. While experimental progress along these two lines is encouraging, large-scale trapped-ion quantum computing is yet to be demonstrated.

In the intermediate term, trapped-ion quantum computing is performed mostly using registers of few to several tens of trapped-ion qubits in a single Coulomb crystal. In these systems, different ions in the register are often individually addressed with focused laser beams. Entanglement is generated using the motional modes of the ion crystal as spin-dependent force mediators between ions. The collective nature of the crystal motional modes leads to all-to-all connectivity between ion qubits. This high connectivity has been shown to be an advantage in comparisons with other qubit technologies [7]. State detection of different qubits in the register is performed in parallel by state-selective fluorescence and the imaging of these photons on a sensitive CCD camera or an array of photon detectors. Only in a few such demonstrations has the ability to perform midcircuit measurement and conditional coherent feedback been shown [3,4,8–14].

Several small trapped-ion quantum registers have been demonstrated and benchmarked in the past few years. Notable examples include Ca^+ registers of optical qubits at the University of Innsbruck and Alpine Quantum Computing [15,16]; Yb^+ registers by the Joint Quantum Institute (JQI), IonQ [17,18], and the Tsinghua group [19]; and shuttling based trapped-ion registers by the National Institute of Standards and Technology (NIST), ETH, Honeywell, and Mainz [10,20–22].

Midcircuit measurements and the ability to coherently operate on qubits conditioned on the measurement outcome are integral parts of many quantum computing protocols, most notably quantum error correction

*Corresponding author. tmanovitz@fas.harvard.edu

†Corresponding author. yotam.shapira@weizmann.ac.il

‡Current affiliation: Department of Physics, Harvard University, Cambridge, Massachusetts 02138, USA.

§These authors contributed equally to this work

Published by the American Physical Society under the terms of the [Creative Commons Attribution 4.0 International](https://creativecommons.org/licenses/by/4.0/) license. Further distribution of this work must maintain attribution to the author(s) and the published article's title, journal citation, and DOI.

(QEC). Midcircuit measurement and coherent feedback in multi-ion crystals present several challenges. First, in state-selective fluorescence, it is necessary to prevent neighboring, quantum information carrying, ions from scattering photons, and thus loss of coherence. In recent demonstrations, this challenge has been addressed by hiding logic ions through encoding them on superpositions in a metastable optical level [15], by using different atomic species as readout and logic ions [10,20] and by shuttling ions to separate measurement regions [20–22]. Second, coherent feedback requires the extraction of the measurement outcome to a classical control system in times shorter than the coherence time of the system. Multi-ion crystals are often read out by cameras that spatially resolve the different ions. Camera-readout schemes are inherently applicable to large ion arrays or to multiple trapping regions and are capable of reading out the state of many arbitrarily positioned ions at once, straightforwardly providing desirable flexibility and scalability that is difficult to match with competing technologies such as photomultiplier tube arrays. Camera readout, however, is often slow; typically, the image is read out from the camera buffer through a universal serial bus (USB) and image processing is done on a personal computer (PC). These processes introduce long latencies, not compatible with real-time coherent feedback. Hence, the realization of scalable mid-circuit readout and coherent feedback with cameras is an outstanding challenge for future ion quantum processors.

Another challenge of quantum computing in multi-ion crystals is to preserve their high fidelity when applied to ion pairs selected from a multi-ion crystal. The higher effective mass of the crystal and the presence of more normal modes renders entanglement gates more susceptible to noise. Recently, robust entanglement gates have been demonstrated using coherent control and dynamic decoupling techniques in two-ion crystals [23–26]. The adaptation of such robust gates to multi-ion crystals is therefore a next important step. A recent publication on an 11-qubit quantum computer has reported the implementation of entanglement gates that are robust against trap-frequency errors [18].

Here, we describe a universal five-qubit trapped-ion quantum computer that realizes two novel features: the incorporation of robust entangling gates and the realization of real-time quantum coherent feedback using a CCD camera. Our computer, constructed at the Weizmann Institute of Science, is based on a single crystal of Sr^+ ions. Qubits are encoded either on optically separated orbitals or in ground-state spin states. We demonstrate midcircuit measurement followed by low-latency coherent feedback using an ion-resolving imaging capability on a CCD camera. Furthermore, we apply two-qubit gates on all ion pairs, using the crystal center-of-mass mode of motion. Our gates are engineered to be robust against gate timing errors and off-resonance carrier coupling. Such small-scale

quantum computing modules are expected to be the building blocks of future large-scale trapped-ion computers and therefore the improvement of their performance is important. Our realization of camera-based midcircuit readout and coherent feedback as well as robust entangling gates is immediately applicable to larger trapped-ion processors.

II. SYSTEM OVERVIEW

Our quantum computer is based on a chain of $^{88}\text{Sr}^+$ ions held in a linear Paul trap. The alkaline earth $^{88}\text{Sr}^+$ possesses a single valence electron, resulting in a simple level structure with optical transitions at convenient visible or near-infrared wavelengths (422, 674, 1092, and 1033 nm), easily generated using diode lasers. The relevant level structure for $^{88}\text{Sr}^+$ includes the ground state $5S_{1/2}$; two long-lived excited states $4D_{3/2}$ (435-ms lifetime) and $4D_{5/2}$ (390 ms); and two short-lived excited states, $5P_{1/2}$ (8 ns) and $5P_{3/2}$ (8 ns). A diagram of these levels is shown in Fig. 1.

Two electromagnetic coils produce a constant magnetic field of 3–5 G in the vicinity of the ions, defining a quantization axis and Zeeman splitting all levels. A qubit can be encoded on the ion in two ways: a Zeeman qubit is encoded using the two Zeeman-split (2.802 MHz/G) spin levels of the ground-state $5S_{1/2}$ manifold, while an optical qubit is encoded by pairing one of the states in this manifold with one of the states of the $4D_{5/2}$ orbital manifold (1.68 MHz/G). We primarily make use of the

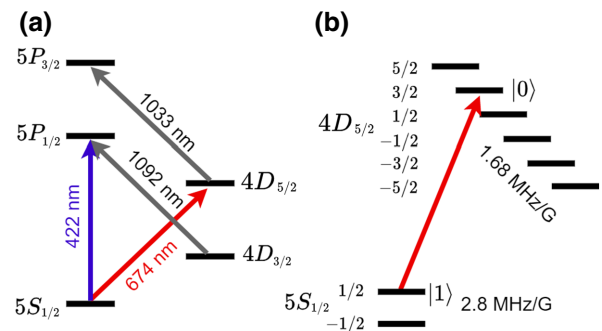


FIG. 1. The $^{88}\text{Sr}^+$ level structure. (a) A 422-nm laser excites the dipole transition from the ground state to the short-lived (8-ns) $5P_{1/2}$ state, used for Doppler cooling, EIT cooling, optical pumping, and state-selective fluorescence-state detection. A 674-nm narrow-line-width laser drives the narrow dipole-forbidden transition between the ground state and the long-lived (390-ms) excited state $4D_{5/2}$, used for sideband cooling and coherent control of the optical qubit. 1092- and 1033-nm lasers are used to repump the $4D_{3/2}$ and $4D_{5/2}$ levels, correspondingly. (b) A magnetic field Zeeman splits all orbitals, including the ground and $4D_{5/2}$ orbitals, which are used to encode an optical qubit. Typically, the qubit is encoded on $|1\rangle = |5S_{1/2}, \frac{1}{2}\rangle$ $|0\rangle = |4D_{5/2}, \frac{3}{2}\rangle$, as shown.

optical qubit. In order to store and protect qubit information during measurement, we encode qubits entirely in the $4D_{5/2}$ orbital manifold. Moreover, in order to selectively hide qubits from interaction with the addressing laser, we may encode these qubits on varying pairs of states in the $5S_{1/2}$ and $4D_{5/2}$ manifolds.

The ions are spatially confined to a one-dimensional chain by a linear Paul trap. A detailed description of our trap and vacuum system may be found in Refs. [27,28]. The trap radio frequency (rf) is at approximately 21 MHz; the secular (harmonic) trapping frequencies are approximately 1–1.5 MHz along the trap axis, corresponding to typical interior spacing of about 3–4 μm , and 3–4 MHz along the radial axes. In order to load ions into the trap, neutral strontium vapor, produced by heating nearby ovens, is photoionized in the trapping region through a two-photon process: the $5s^2\ ^1S_0$ ground state is excited to the $5s5p\ ^1P_1$ state and then to the self-ionizing $5p^2\ ^1D_2$ state, using corresponding 461-nm and 405-nm lasers.

Optical control of the ions is realized using lasers at wavelengths of 422 ($5S_{1/2} \leftrightarrow 5P_{1/2}$), 674 ($5S_{1/2} \leftrightarrow 4D_{5/2}$), 1033 ($4D_{5/2} \leftrightarrow 5P_{3/2}$), and 1092 nm ($4D_{3/2} \leftrightarrow 5P_{1/2}$). Lasers enter the vacuum chamber through fused-silica windows on the sides or the top of the chamber. All lasers are generated by diodes in an external-cavity diode laser (ECDL) configuration and are locked to stable external references. Of particular importance is the 674-nm laser, which is used to coherently control the optical qubit. This laser is first locked to a ultralow-expansion (ULE) Fabry-Perot cavity with high servo bandwidth; in order to filter out the lock servo bumps, the cavity transmission is amplified by a slave diode and the output is then locked to an additional temperature-stabilized ULE Fabry-Perot cavity, generating narrow-line-width light [29].

The ion chain is typically Doppler cooled to a temperature of a few millikelvins using the 422-nm laser, together with a 1092-nm laser to repump the long-lived $4D_{3/2}$ orbital. The chain may then be further cooled to the ground state of several or all motional modes using sideband and electronically-induced transparency (EIT) cooling. Sideband cooling is used to cool axial motional modes and is performed by tuning the 674-nm laser near the red-sideband resonance of the relevant mode, together with the 1033-nm repump and 422-nm optical pumping lasers. Several modes may be cooled in parallel by driving the 674-nm laser using multiple frequencies. EIT cooling is used to cool all radial modes in parallel. A 422-nm σ^+ -polarized pump and π -polarized probe isolate an effective Λ -type three-level system with a k vector that is perpendicular to the trap axis and equally overlaps both radial trapping axes. Blue detuned from the transition, the pump creates a narrow asymmetric (Fano) resonance when addressed by the probe beam, enabling efficient cooling with low background scattering [30]. The layout of the trap and laser configuration is illustrated in Fig. 2.

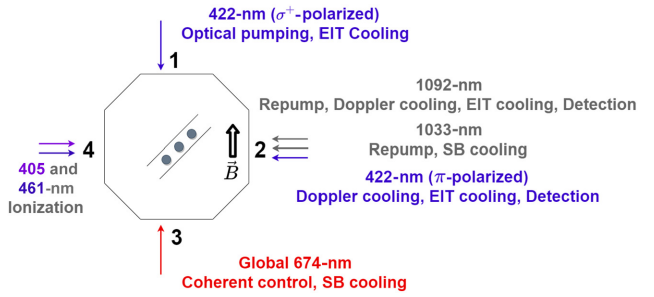


FIG. 2. Our trap is set in an optically accessible octagonal vacuum chamber. The quantization axis is defined by a pair of coils. Both a 674-nm beam, used for global coherent control and sideband (SB) cooling, as well as a circularly polarized 422-nm beam, used for optical pumping and EIT cooling, propagate along the quantization axis. 405- and 461-nm beams are used to ionize neutral Sr vapor and generate ions for trapping. 422-nm light for detection, EIT cooling, and Doppler cooling, as well as two repump lasers, enter the chamber from a single port. Not shown is the 674-nm individual addressing path, used for single-ion coherent control, which enters the chamber from a recessed window in the top.

Qubit initialization and measurement are realized using the 422-nm laser, together with the 1092-nm repump laser to prevent pumping into the long-lived $4D_{3/2}$ orbital. The qubits are prepared in the qubit ground state $|1\rangle = |5S_{1/2,+1/2}\rangle$ by optical pumping using a σ^+ polarized 422-nm beam. This process prepares $|1\rangle$ with an error smaller than 10^{-3} within 10 μs . Strong measurement of the optical qubit is achieved by state-selective fluorescence: ions are illuminated with the light, which scatters off ions occupying $|1\rangle$ but not off those occupying the qubit excited state $|0\rangle = |4D_{5/2,+3/2}\rangle$ (or any other state in the $|4D_{5/2}\rangle$ manifold). The scattered fluorescence is imaged onto an electron-multiplying CCD (EMCCD) camera, from which the state is determined for each ion separately. Fluorescence is collected for 1 ms, giving rise to an error of 2.6×10^{-3} due to the finite lifetime of $|0\rangle$.

Coherent operations are performed with either the 674-nm laser (optical qubit) or an rf magnetic field (Zeeman qubit). The latter is induced by running rf current through an electrode that is 2 mm away from the ions and is used to drive transitions between Zeeman states within the $5S_{1/2}$ and $4D_{5/2}$ manifolds. A narrow-line-width [29] 674-nm laser, illuminating the ions through a global and an individual addressing path, is used to drive coherent optical-qubit operations. The global path overlaps all ions in the chain with approximately uniform intensity. By resonantly addressing the ions, this path can be used to apply global unitary rotations of the form

$$U_G(\phi, \theta) = \exp\left(i\frac{\theta}{2} \sum_i \sigma_i^\phi\right). \quad (1)$$

Here, $\sigma_i^\phi = \cos(\phi)X_i + \sin(\phi)Y_i$, while X_i and Y_i are the standard Pauli operators acting on the optical-qubit subspace of ion i . Using the Mølmer-Sørensen interaction, the global path can also be used to generate global entangling operations of the form

$$U_{MS}(\phi, \theta) = \exp\left(i\frac{\theta}{2} \sum_{i<j} \sigma_i^\phi \sigma_j^\phi\right). \quad (2)$$

The individual addressing path is tightly focused onto a single ion at a time and can be quickly steered between ions using a pair of acousto-optic deflectors (AODs) in an XY (perpendicular) configuration. For this path, the laser is tuned off resonance to generate a light shift, and can therefore realize the operations

$$U_i(\theta) = \exp\left(i\frac{\theta}{2} Z_i\right). \quad (3)$$

Here, Z_i is the standard Pauli operator acting on the optical-qubit subspace of ion i . Together, these $U_G(\phi, \theta)$, $U_{MS}(\phi, \theta)$ and $U_i(\theta)$ operations constitute a universal gate set on the optical-qubit register. Below, we describe our implementation of entangling and individual addressing operations in more detail.

III. INDIVIDUAL-QUBIT ADDRESSING AND DETECTION

Universal quantum computation requires the ability to both operate on and measure the state of any specific qubit in the register. In ion traps, the interion spacing of a few micrometers [31] is larger than optical wavelengths, implying that one can use focused laser beams for resolving the position of each ion in the chain [15, 17, 32]. However, while larger than optical wavelengths, interion spacing is not *much* larger, meaning that high numerical apertures (NAs) are necessary and no more than minor aberrations can be tolerated for individual addressing to work with sufficiently low crosstalk error. Other approaches to individual addressing include spectrally resolving ions [33–35], coupling ions to spatially varying oscillating fields [36], or shuttling them to separate trapping regions [2–4]).

We perform both qubit-resolving state measurements as well as individual addressing for single-qubit rotations using the same high-resolution optical system. Qubits are measured by collecting state-selective fluorescence on the $5S_{1/2} \leftrightarrow 5P_{1/2}$ transition at 422 nm, which is imaged onto an EMCCD camera (Andor iXon Ultra 897). We individually address qubits by shining 6740nm light, near resonant with the optical $5S_{1/2} \leftrightarrow 4D_{5/2}$ transition, in a tightly focused beam that spatially overlaps only a single ion at a time. The laser beam is quickly steered between ions using two orthogonal AODs.

The imaging system objective (LENS-Optics) has an effective focal length of 30 mm and a NA of 0.34, and is designed to correct for chromatic aberrations of its lenses as well as the vacuum-chamber fused-silica windows at both relevant wavelengths (422 nm for detection and 674 nm for addressing). The objective is mounted on a Newport xyz translation stage for positioning, which is itself connected to a custom-made holder that is tightly anchored to the vacuum-chamber flange. This allows the objective to be positioned a few millimeters away from the vacuum-chamber window, which is sunken into the chamber and enables an effective working distance of 30 mm from the ions. Anchoring the objective to the chamber minimizes vibrations relative to the ion position, suppressing beam-pointing noise, which can be significant for tightly focused beams. The objective is designed to work with the ions in its focal plane using a $\infty - f$ configuration. We slightly shift the objective away from this working point so that it directly images the ions on the EMCCD at a distance of approximately 120 cm. This enables imaging of the ions without adding any additional optical elements, thus reducing aberrations.

Apart from the camera, all other optical elements are positioned on an optical breadboard mounted directly above the trap by five aluminum legs. Diagonal brace beams are added where possible to mitigate table vibrations. A 1.5-in.-diameter hole is bored through the table, directly above the objective and the trap. A pair of mirrors change the optical beam path from the horizontal path on the breadboard onto the vertical path descending into the trap and vice versa. Near these mirrors, a long-pass dichroic mirror separates the detection and addressing beam paths [37].

A. Individual addressing

The narrow-line-width 674-nm light is passed through a double-pass AOD and a single-pass acousto-optic modulator (AOM) that provide amplitude and phase control. The light is then delivered with an optical fiber to the optical breadboard on which it passes through a pair of Isomet OAD948-633 AODs, held in an XY configuration. The zero-order diffraction of the second AOD is picked up by a detector; the signal from this detector is sent to control electronics that regulate an attenuator on the rf for the single-pass AOM in the 674-nm individual addressing line and is used to stabilize the laser power. The diffracted light passes through a pair of lenses, followed by the dichroic mirror, and is focused onto the ions by the objective lens.

The AODs are chosen to support the contradictory demands of high resolution and short switching time. The switching time τ_s is determined by the propagation time of the acoustic wave through the laser waist of size d on the AOD: $\tau_s = d/v$, where v is the acoustic velocity. The resolution N , defined as the number of resolved optical spots

that the deflector can scan, is given by $N = \tau_s \Delta f$, where Δf is the frequency bandwidth of the AOD. Hence, the resolution can be increased at the cost of longer switching times. The Isomet AODs provide a bandwidth $\Delta f = 45$ MHz and an acoustic velocity of $v = 650$ m/s. Hence, a spot size of 1.1 mm defines switching time $\tau \approx 1.7 \mu\text{s}$ and resolution $N \approx 77$.

The AODs are set in an XY configuration so that the beam can be scanned across a plane, rather than a line, enabling precise positioning of the beam focus on each ion. The orientation relative to the trap is such that the ion chain corresponds to a 45° angle with respect to axes defined the XY configuration and opposite frequencies are added to the two AODs in order to scan across the ion chain. Such a configuration simplifies control, as the 674-nm frequency does not need to be corrected when the focus position is changed from one ion to another. Taking the XY configuration into account, the resolution is effectively increased to $N \approx 108$. These parameters are sufficient, as they support a low time overhead compared to single-qubit gates (approximately $10 \mu\text{s}$) and can easily accommodate a large ion chain ($< 30 \mu\text{m}$).

The individual addressing system is used to address the ions off resonantly, generating a light shift with effective Rabi frequency $\Omega_{\text{LS}} = \Omega_{\text{res}}^2/2\Delta$, where Ω_{res} is the

resonant Rabi frequency and Δ is the detuning from resonance. Typical parameters are $\Omega_{\text{res}} = 500$ kHz and $\Delta = 5$ MHz, implying an effective light shift of $\Omega_{\text{LS}} = 25$ kHz. Limiting the individual path to σ_z rotations via off-resonant illumination has significant advantages as compared with resonant coupling. Coherent resonant coupling from both global and individual paths requires the maintenance of phase coherence between the two, which is challenging due to the very different optical trajectories. Furthermore, off-resonant addressing minimizes crosstalk by effectively decreasing the individual path spot size. While the resonant coupling strength is determined by the Rabi frequency Ω_{res} , the off-resonant coupling is proportional to Ω_{res}^2 ; hence the effective beam cross section depends on the amplitude squared rather than the amplitude and leads to a $\sqrt{2}$ narrower cross section. σ_z rotations in conjunction with σ^ϕ global rotations can generate any single-qubit unitary.

We characterize the beam profile by measuring the light shift on the ion, which is proportional to the laser intensity, as a function of the AOD frequency or, correspondingly, the beam position. The results are shown in Fig. 3. A useful measure of the spot size is the beam-waist diameter $2w_0$, which is the $1/e^2$ intensity diameter of a Gaussian beam. Making use of the full aperture of our 0.34 NA objective, for a diffraction-limited beam, one would

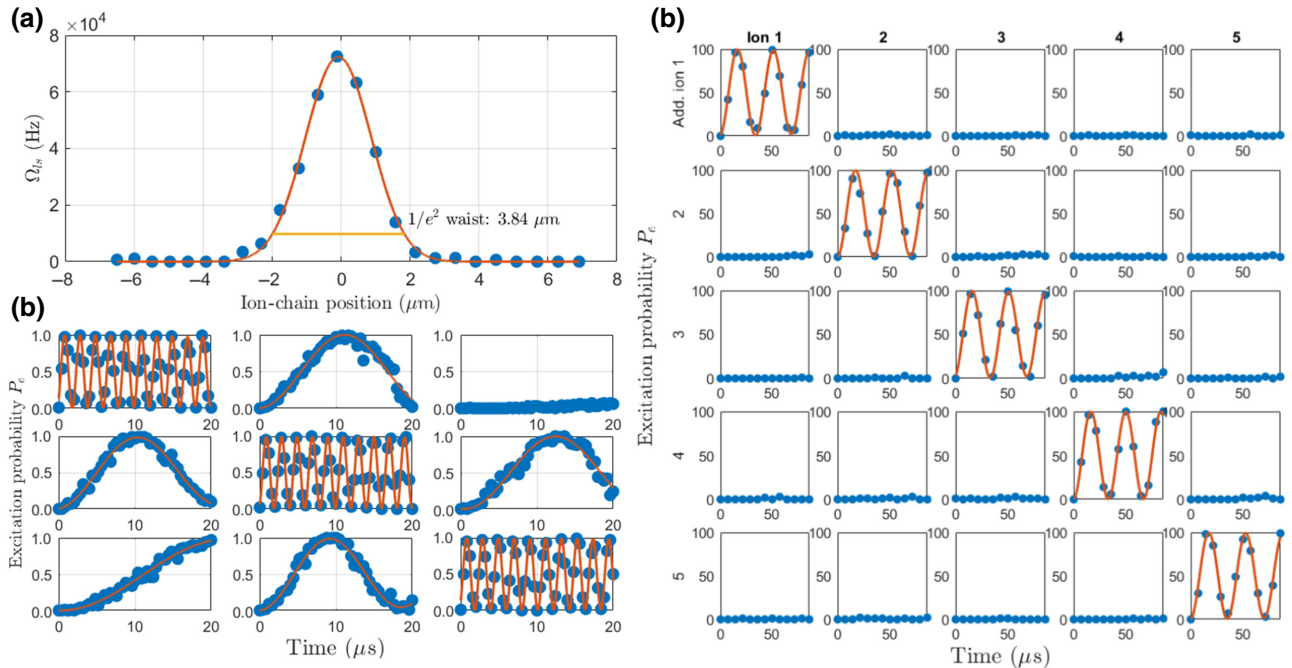


FIG. 3. (a) The beam-intensity profile of the individual addressing beam along the ion-chain axis, determined by measuring the position-dependent Ω_{LS} , which is proportional to the intensity. We measure a $1/e^2$ waist diameter of $2w_0 = 3.84 \mu\text{m}$. (b) In order to characterize the individual addressing beam, we measure crosstalk on a three-ion chain. We artificially increase crosstalk by resonantly addressing the ions. The crosstalk Rabi frequency ratio is approximately 10^{-1} for a $3.7\text{-}\mu\text{m}$ interion distance. (c) A demonstration of single-qubit Rabi oscillations using individual addressing in the light-shift configuration. Here, we use a five-ion quantum processor, with a minimal interion distance of $2.8 \mu\text{m}$. Each column represents one of the five ions, in appropriate order, and each row represents an attempt to address the corresponding ion (e.g. the top row depicts the attempt to address ion 1).

expect a beam-waist diameter $2w_0 = 2\lambda/\pi NA \approx 1.3 \mu\text{m}$. However, we measure a significantly larger beam-waist diameter of $2w_0 = 3.84 \mu\text{m}$. The discrepancy is a result of an effectively smaller NA and aberrations. Use of the entire aperture of the objective would clip the outer tail of the Gaussian profile; this would imply a focus on the ions that is a convolution of a Gaussian and an Airy beam profile. The latter introduces intensity oscillations that decay with distance from the beam center r as $1/r^2$, which may then generate non-negligible crosstalk between ions. To avoid significant Airy-like features, the beam-waist diameter on the objective is set to be smaller than the objective aperture, implying an effective NA of approximately $NA \approx 0.19$, which, for a diffraction-limited spot, would result in a waist diameter $2.3 \mu\text{m}$. In practice, we achieve a diameter that is approximately 1.7 times larger due to aberrations, which are captured by a beam-quality parameter $M^2 \approx 1.7$.

As long as the distance between ions is larger than the beam-waist radius of $w_0 = 1.92 \mu\text{m}$, which is always true for our experiments, the crosstalk is determined by the beam tail. Perfectly Gaussian beams decay strongly, so in practice tails are dominated by small aberrations, such as weak Airy contributions from the aperture cutoff, or minor astigmatism and coma from imperfect alignment. Hence, the beam waist is not necessarily a reliable parameter for evaluating crosstalk. The crosstalk parameter of interest is $R_{\text{LS}} = \max_{i,j} (\Omega_{\text{LS}}^{ij}/\Omega_{\text{LS}}^{ii})$, where Ω_{LS}^{ij} is the light shift induced on ion j when attempting to address ion i . R_{LS} can be used to give an upper bound on errors generated by crosstalk per single-qubit operation: $\epsilon_{\text{crosstalk}} \leq 2R_{\text{LS}}^2$ (under the assumption that nearest-neighbor crosstalk is the main source of error). As the R_{LS} is quite low, it is difficult to properly measure directly. Instead, we measure the resonant crosstalk parameter $R_{\text{res}} = \max_{i,j} (\Omega_{\text{res}}^{ij}/\Omega_{\text{res}}^{ii})$, from which one can straightforwardly derive $R_{\text{LS}} = R_{\text{res}}^2$. To do so, we trap a three-ion chain with interion distances $3.7 \mu\text{m}$ (a typical interion distance for small chains in our trap), drive resonant Rabi oscillations while attempting to address each ion, and measure the Rabi frequency on all ions simultaneously. The results are shown in Fig. 3. For an interion distance of $3.7 \mu\text{m}$, we measure $R_{\text{res}} = 0.12(1)$, implying $R_{\text{LS}} = 0.014(2)$ and $\epsilon_{\text{crosstalk}} \leq 3.9(5) \times 10^{-4}$. Hence, for such interion distances, the error induced by crosstalk is significantly lower than other error sources. An example of single-qubit Rabi rotations in a five-qubit chain, induced by light-shift individual addressing, is shown in Fig. 3(c), with no discernible crosstalk.

The error incurred by an individual addressing operation on one of the ions is not limited to crosstalk; indeed, we find that it is dominated by other terms. We measure the fidelity of an individual addressing $\sigma^z \pi$ angle rotation. This is achieved by initializing the three ions in a $|111\rangle$ state, applying a global $\sigma^x \pi/2$ pulse, followed by an individual addressing $\sigma^z \pi$ pulse on one of the ions and then

a global $\sigma^x - \pi/2$ pulse (applied by varying the phase of the global 674-nm laser by π). The desired result is a chain in which only one of the qubits is in the excited state, e.g., the $|101\rangle$ state. After correcting for state-preparation-and-measurement (SPAM) errors due to the global shelving pulses, optical-pumping initialization, and measurement fidelity, we arrive at a fidelity of $0.9964(10)$ for a $\sigma^z \pi$ pulse. We also find that while the target ion undergoes an operation, other ions suffer an error of $0.001 - 0.002$ per ion; this may be due to background σ^z noise.

B. Detection

Qubit-state detection is performed through state-selective fluorescence scattering of the 422-nm laser on the $5S_{1/2} \leftrightarrow 5P_{1/2}$ transition: fluorescence is observed only if the electron collapses to the $5S_{1/2}$ state. The scattered fluorescence is picked up by the LENS-Optics 0.34 NA objective, which focuses the images of the ions directly onto an Andor iXon Ultra 897 EMCCD camera, placed approximately 1230 mm away from the objective. This results in a magnification of about $\times 41$, measured by comparing the distance between ions on camera to calculated values [31]. Apart from the objective itself and aligning mirrors, the only optical element in the path of fluorescence light is a dove prism; the prism is used to rotate the chain image such that it is aligned horizontally on the EMCCD and is parallel with the pixel axis, allowing for a smaller pixel region of interest (ROI) and hence faster readout. The camera is placed on a custom-made holder, physically separated from any other element in the system, in order to suppress detrimental acoustic vibrations caused by the camera cooling fans.

The main advantage of camera detection is the spatial resolution that it provides, allowing for simple differentiation between ions. Beyond the optical resolution, the iXon Ultra has high quantum efficiency; high readout speeds for a CCD camera; thermoelectrically cools the CCD array to -90°C , substantially mitigating thermal detection noise; and possesses an electron-multiplying capability that can increase the gain to $\times 500$. These attributes are important advantages for ion detection, giving good signal-to-noise ratios (SNRs) for short detection times. However, the iXon Ultra uses a masked CCD storage area (designed to improve duty cycle); transferring the signal through the additional CCD frame storage area implies a readout time overhead of approximately $300-400 \mu\text{s}$.

Typically, we define a rectangular ROI on the camera of approximately $6 \times (20 - 40)$ pixels, where the latter depends on the number of ions in the chain. Vertically smaller ROIs result in lower readout times for the camera and are thus beneficial. Readout times can be further minimized by placing the ion-chain image in the corner of the pixel array that is closest to the analog-to-digital-converter (ADC). We achieve typical readout times (not

including the detection exposure time itself) of 600–700 μs including the frame storage overhead.

During a standard calibration procedure, a set of 1500 images of the ions fluorescing and 1500 images of the ions not fluorescing are acquired. Then, using these images, a set of pixels are allocated to each ion. For each ion, the distributions of the signal sum on the corresponding pixels are compared for the fluorescing and nonfluorescing case and an intermediate value is chosen as a threshold discriminator. After calibration, for every measurement and for every ion, the pixel sum is compared to this threshold in order to differentiate the fluorescing state (implying $|1\rangle = 5S_{1/2}$) from a nonfluorescing state (implying $|0\rangle = 4D_{5/2}$).

For exposure times of 1 ms, we find that detection error is dominated by spontaneous emission of the $4D_{5/2}$ orbital, giving a detection error of $1 - e^{-1/390} \approx 2.6 \times 10^{-3}$. We perform 2×10^4 detection measurements, where the ion state is predetermined by the application, or lack thereof, of the 1092-nm repump laser. When this laser is turned off, spontaneous emission errors are practically undetectable; if an emission event occurs, the electron is quickly pumped back into the nonfluorescing $4D_{3/2}$ state and remains there until another emission event or the end of the measurement. With spontaneous emission suppressed, we find no errors for these 2×10^4 measurements, implying with high confidence an error rate lower than $< 10^{-3}$ from other sources. Thus we conclude that the spontaneous emission error is dominant.

For a series of acquisitions, each image is read via the ADC and saved in the internal buffer of the camera. The buffer is read out at the end of the series by a USB, where the measurement results are determined retroactively through the simple image analysis described above. In certain scenarios (e.g., QEC), determining the measurement result retroactively is not good enough and a real-time decision must be made. We achieve this as well with the Andor iXon camera, as described in a succeeding section detailing our real-time quantum coherent feedback module.

IV. ROBUST ENTANGLING GATES

Entangling gates are a key component in any realization of a quantum computer. They are typically the most challenging gates of the universal gate set and in ion quantum processors are often substantially slower and less robust than single-qubit operations. The most prevalent method to entangle qubits in an ion-trap quantum processor is by using the Mølmer-Sørensen (MS) technique [38,39] in which a spin-dependent force is exerted on a collective normal-mode of motion of the ion chain, resulting in an effective qubit-qubit interaction.

MS gates are very successful in two-ion chains [40–43]. However, in long ion chains, the gates have an increased sensitivity to even small implementation imperfections.

Here, we utilize an entangling-gate technique that employs coherent control in order to decrease the sensitivity of the gate operation to experimental imperfections [23,24]. This technique is an extension of the MS gate and is beneficial for scaling up the ion-qubit register. We demonstrate our entangling scheme on pairs of ions in a five-ion chain and, in addition, as an all-to-all gate in a four-ion chain.

Our method is based on driving the gate with a multi-tone laser that is tuned on resonance with the optical-qubit transition along with a sequence of amplitude modulations at frequencies $\omega_j = \nu + n_j\xi$, where ν is the frequency of the normal mode of motion used to mediate the interaction, n_j is an integer, and ξ is a detuning, such that the gate time is $T = 2\pi/\xi$. One may write the interaction Hamiltonian due to this driving field as

$$V = \frac{1}{2}\Omega \sum_i \sigma_i^x \cos(kx_i - \omega_{eg}t) \sum_j r_j \cos(\omega_j t). \quad (4)$$

Here, Ω is the resonant Rabi frequency, σ_i^x is the Pauli operator on the optical-qubit subspace of ion i , k is the optical wave number, x_i is the position of ion i , ω_{eg} is the resonant frequency for the optical-qubit transition, and r_j represents the magnitude of the amplitude modulation at frequency ω_j . The regular MS gate is formed by the special choice of a single modulation frequency with $n = 1, r = 1, \xi = 2\eta\Omega$, and $\eta = kx_0$, where x_0 is the ground-state extent of the relevant motional mode.

A derivation similar to that found in Ref. [23] shows that the fidelity of a two-ion entangling gate in an N -ion chain is given by

$$F_{2,N} = \frac{1}{8} \left\{ 4e^{-\frac{F^2+G^2}{2}(\bar{n}+\frac{1}{2})} \cos \left[N \left(A + \frac{FG}{2} - \frac{\pi}{2} \right) \right] \right. \\ \times \cos \left(A + \frac{FG}{2} - \frac{\pi}{2} \right) + e^{-2(F^2+G^2)(\bar{n}+\frac{1}{2})} \\ \left. \times \cos \left[2N \left(A + \frac{FG}{2} - \frac{\pi}{2} \right) \right] + 3 \right\}, \quad (5)$$

where $G + iF = \int_0^T dt \sum_j r_j e^{in_j\xi t}$, $A = -\int_0^T dt gF$, and \bar{n} is the mean occupation of the normal mode, assuming an initial thermal state. Expanding Eq. (5) in powers of N , we find that for a MS gate, the infidelities due to an inaccurate gate time, T , or normal-mode frequency, ν , scale quadratically with N . Thus, the use of a gate that is robust to these types of errors is necessary for scaling up the ion-trap quantum processor. Similar scaling laws occur for N -qubit all-to-all entangling gates. Furthermore, the gate time typically scales as \sqrt{N} , resulting in an even increased sensitivity to errors, which can be mitigated only by coupling to additional normal modes of motion of the ion chain [44].

By choosing $\{n_j, r_j\}$ correctly, one can use the additional degrees of freedom to suppress unwanted sources

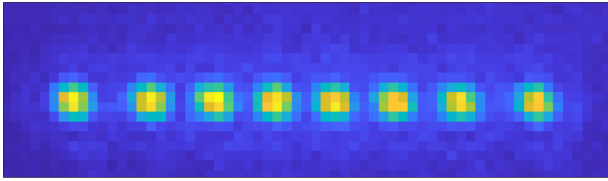


FIG. 4. An image of an eight-ion chain on the iXon Ultra camera. Here, the minimal interion distance is about $2.3 \mu\text{m}$. The ion chain is aligned along the pixel axis using a dove prism set before the camera.

of infidelity, in an order-by-order manner. In our quantum information processor, we use two modulation terms rather than one, which leads to a cardioid-shaped trajectory of the normal-mode in phase space. A cardioid gate eliminates the leading-order contribution of carrier coupling and errors due to timing inaccuracies and reduces errors due to normal-mode frequency inaccuracies and normal-mode heating.

While the most efficient implementation uses harmonics $n_j = 1, 2$, we realize the technique with the harmonics $n_j = 2, 3$ or $n_j = 1, 3$, in order to avoid errors caused by spurious frequencies due to third-order nonlinearities in the AOM or the rf amplifier. The double amplitude modulation is equivalent to a four-frequency field that is generated by driving an AOM with rf generated by a Keysight Trueform 33622a arbitrary waveform generator (AWG).

In addition to the cardioid modulation, we implement a Hahn echo pulse midway through the gate operation. For the MS gate, this implies a prolongation of the gate time by a factor of $\sqrt{2}$ but increases the gate robustness to σ^z noise, which is our main source of decoherence. As the noise does not commute with the gate Hamiltonian, the echo pulse cannot completely suppress even dc noise. However, echo pulses can mitigate σ^z error to some degree, as shown in Ref. [26].

In order to characterize the fidelity of our entangling gates, we implement two-qubit cardioid gates on all pairs of qubits in a five-qubit chain. We encode qubits on the $|1\rangle = 5S_{1/2,1/2}$ and $|0\rangle = 4D_{5/2,3/2}$ states and use the $|\tilde{1}\rangle = S_{1/2,-1/2}$ and $|\tilde{0}\rangle = 4D_{5/2,-3/2}$ states as a “hidden subspace”; qubits encoded on the latter are spectrally decoupled from the entangling interaction. For each qubit pair, we first prepare the register in the $|11111\rangle$ state using optical pumping. We use individual addressing and global 674 nm pulses, as well as rf pulses on the Zeeman qubit, to hide all qubits but the targeted pair onto their corresponding hidden subspace, producing the state $|\tilde{1}\tilde{1}\rangle \otimes |11\rangle$, where the latter two represent the target qubits. We then carry out a global cardioid gate with an echo pulse, ideally producing the maximally entangled Bell state $|\psi_{\text{Bell}}\rangle = 1/\sqrt{2}(|11\rangle + i|00\rangle)$ for these two qubits. We measure the state fidelity resulting from this procedure by measuring the populations and coherence of this two-qubit state through a parity scan.

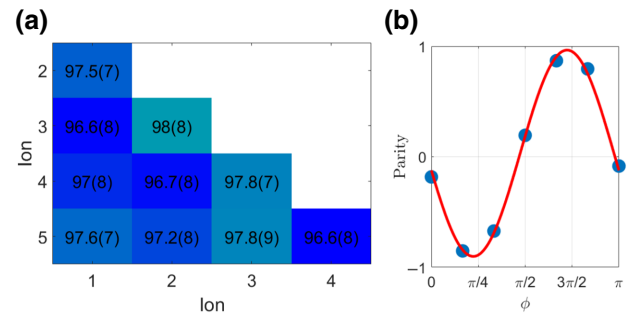


FIG. 5. (a) Fidelities for generating a two-qubit maximally entangled state by applying an entangling gate for every pair of qubits on a five-ion chain. The values are SPAM corrected, with an average fidelity of $0.973(2)$. The entangling gate is a cardioid (1,3) Mølmer-Sørensen, applied with an echo pulse midway through the gate. (b) An example parity measurement on a pair of qubits in the chain.

The results of our measurements are summarized in Fig. 5. After correcting for the preparation cost of hiding three out of five ions, measured independently, as well as state-measurement error, we reach an average fidelity of $0.973(2)$. The gate duration, including the $\sqrt{2}$ prolongation implied by the echo-pulse addition, is approximately $200 \mu\text{s}$. These fidelities are comparable with those reported by leading state-of-the-art trapped-ion quantum computers [32,45]. We believe that our major source of error is due to magnetic σ^z noise, which is only partially mitigated by the echo pulse, as the optical-qubit coherence time is limited to approximately 2 ms, only a single order of magnitude longer than the gate time. Hence, we expect significant improvements in fidelity with straightforward improvements to our experimental setup, such as the addition of a μ -metal shield.

We apply these gates with trap frequencies of 1 MHz along the trap axis and approximately 4 MHz along the radial axes. The heating rate for the axial center-of-mass (COM) mode, which mediates the interaction, is approximately $100 \bar{n}/\text{s}$, implying a heating of approximately $0.02\bar{n}$ during the gate, which, due to the robustness of MS gates to temperature, negligibly affects fidelity. Other possible noise sources include high-frequency laser phase noise, which may generate incoherent driving of the carrier transition.

Using the same methods described above, we also implement a cardioid all-to-all gate on a $N = 4$ ion chain and compared it with a conventional MS gate. Figure 6 shows the dynamics of four ions under the MS (top) and cardioid (bottom) all-to-all entanglement gates. The robustness of the cardioid gate to pulse-time errors is apparent, as the evolution in the vicinity of $t = T$ is much smoother than that of the MS gate. Furthermore, the dynamics generated by the cardioid gate are closer to the ideal case compared to MS.

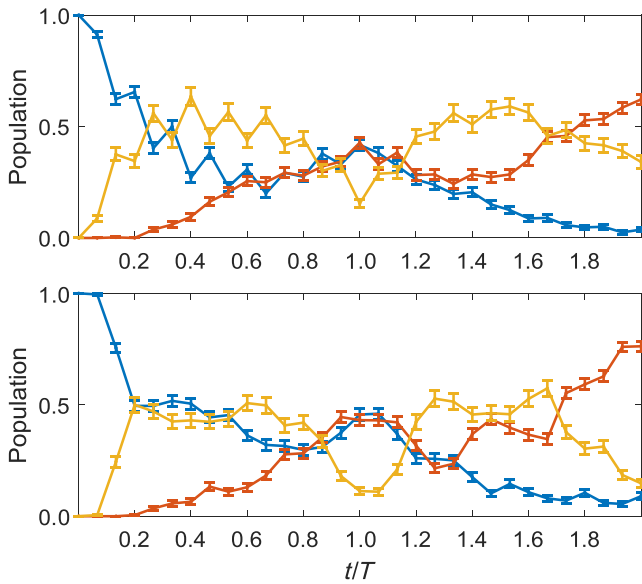


FIG. 6. The populations of the ground state, $|1111\rangle$ (blue), and of the fully excited state, $|0000\rangle$ (red), are shown. The system is initialized at $t = 0$ to the ground state. Ideally, the population of these states at gate time, $t = T$, is 0.5, implying a maximally entangled qubit state. In addition, the population of the 14 remaining states is shown (yellow). Ideally, the population of these states at gate time is zero, indicating that the qubit state is disentangled from the motion. The error bars reflect shot noise due to 400 repetitions of each evolution time. In the MS gate (top), the population changes sharply at the gate time, indicating an increased sensitivity to pulse timing, while the cardioid gate (bottom) approaches the gate time smoothly, indicating a robust gate. Furthermore, the cardioid gate generates populations that are closer to the ideal case, due to reduced carrier coupling.

To further demonstrate the robustness of the cardioid gate to pulse-time errors, we measure the gate fidelity at different evolution times. Figure 7 compares the four-qubit gate fidelity of the cardioid (blue) and MS (red) gates. Clearly, the cardioid gate exhibits a higher fidelity, which is also less sensitive to incorrect gate times. The peak fidelities are 0.84(3) and 0.69(3) for the cardioid and MS gates, respectively. The all-to-all gate fidelity is notably lower than that of the two-qubit gates, primarily due to increased susceptibility to σ_z noise.

V. COHERENT FEEDBACK

Neither complete isolation of a quantum computer from the environment nor perfectly executed unitary operations are physically realizable goals and errors will inevitably decohere the quantum computer states. Fortunately, a family of techniques known as QEC can enable fault-tolerant quantum computation for arbitrarily long computations given low enough error rates [46,47]. QEC protects quantum information by encoding it nonlocally, using highly entangled states. As the information is encoded over

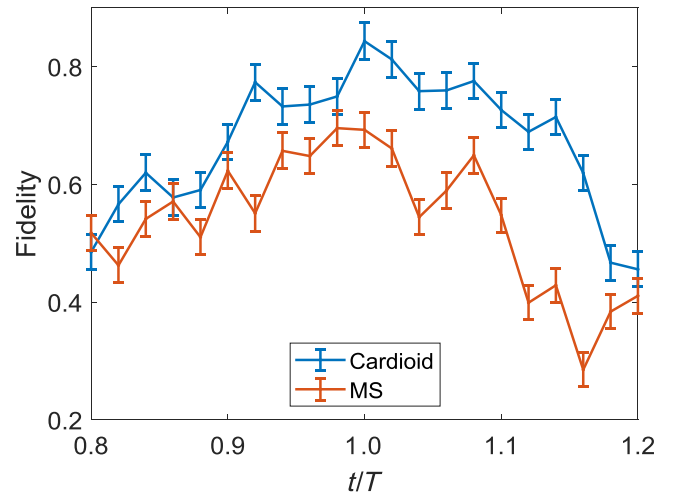


FIG. 7. The state fidelity for a four-qubit Greenberger-Horne-Zeilinger (GHZ) state generated by the cardioid (blue) and MS (red) gates is measured for different gate times. The cardioid gate exhibits a higher peak fidelity and reduced sensitivity to pulse-time errors compared to MS.

high-order correlations, the otherwise harmful local noise does not destroy information and the errors that it inflicts can therefore be rectified.

QEC requires measuring parts of the qubit register while maintaining the quantum coherence of the rest and generating feedback operations conditioned on the measurement results. Generally, this is a technically difficult task: measurement is a highly dissipative process, strongly coupling parts of the quantum computer to the environment; at the same time, other (often neighboring) parts of the computer must remain completely decoupled from the environment. Furthermore, the measurement must be read out, and a conditional operation must be applied, all within the coherence time of the system.

Standard state-selective fluorescence detection on an EMCCD camera is ill equipped to fulfill these demands. Photon scattering from a laser beam overlapping the entire chain collapses the wave function of all qubits in the register. Even if the measurement beam is focused onto single ions, since photon collection is limited, typically thousands of photons have to be scattered before the state of the ion can be inferred with sufficient statistical certainty. Secondary photon scattering will lead to errors on other ions with high probability.

Furthermore, the readout of EMCCD cameras is typically slow, since the transfer of charge across the camera pixel array takes time. Thus, in most camera-based readout, the processing of the detection results is done retroactively. Experiments are almost always repeated many times and in each iteration the image acquired by the camera is saved onto a buffer. Only after all iterations are complete is the entire set of images transferred from the buffer to a

computer via USB, where image processing is performed to determine the measurement results. This retroactive processing is not adequate for real-time coherent feedback. Since the USB interface is slow and ultimately controlled by the CPU, simply reading out each measurement individually is not a viable solution to this problem. Furthermore, after readout, each image must be processed quickly and the result should be fed back into the system within the coherence time of the qubits.

In order to address these challenges, we develop a module and a procedure for live readout and real-time quantum-coherent feedback in our system. In order to measure only preselected qubits, we use individual addressing pulses to “hide” all other qubits by encoding them in levels that are completely decoupled from 422-nm scattering and therefore from the measuring process. This is achieved by making use of another state in the six-dimensional Zeeman manifold of the $4D_{5/2}$ orbital. Specifically, while qubits to be measured remain encoded on the optical-qubit states $|1\rangle = |5S_{1/2,1/2}\rangle$ and $|0\rangle = |4D_{5/2,3/2}\rangle$, hidden qubits are encoded into the $|\bar{0}\rangle = |4D_{5/2,-3/2}\rangle$ and $|\bar{1}\rangle = |4D_{5/2,3/2}\rangle$ states [see Fig. 9(a)]. The hiding process is realized using a series of rf and optical pulses, as shown in Fig. 9(b). After the hiding protocol, we measure the remaining qubits by turning on the 422- and 1092-nm lasers, performing our standard measurement protocol, but reading out and processing the results in real time. Then, the hiding process is reversed and an operation conditioned on the measurement result can be applied.

To implement real-time readout, processing, and feedback, we realize a scheme that completely bypasses the camera buffer, the USB readout, the retroactive image processing, and, in fact, any PC involvement. Fast readout is enabled by the Camera-Link port of the iXon Ultra camera. Camera-Link is a communication protocol that is designed for fast reading of images, and in the iXon Ultra outputs data before they reach the camera buffer. The acquired image is read out and processed in real time by a dedicated frame-grabber FPGA (National Instruments NI-PCIE-1473R), which comes with a built-in Camera-Link port. The frame grabber can perform image processing on the Camera-Link data on the fly, while information is still arriving. In this way, decisions on the outcome of the measurement, expressed as a bit state for each qubit, are made very quickly and, for some cases, qubit states are inferred before the complete image has even been read out by the ADC. The processing algorithm is preconfigured on the frame-grabber FPGA in advance and is identical to the algorithm realized in PC image processing: a set of pixels and a threshold value are allocated to each ion; for every image, the frame grabber sums over the values on pixels ascribed to each ion and determines whether the result is larger than the corresponding threshold value; a binary string with the length of the ion chain is given as output.

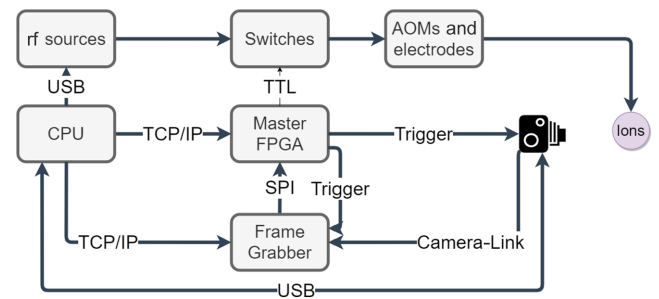


FIG. 8. The control scheme for the quantum coherent feedback module. The user controls the experiment using the CPU, which through the USB determines the parameters for the rf sources and the camera and via TCP/IP uploads the detection parameters to the frame-grabber field-programmable gate array (FPGA) and an experimental sequence onto the main FPGA. Once started, the main FPGA executes the sequence by controlling a set of transistor-transistor logic (TTL) digital outputs, which can turn on or off electromagnetic fields addressing the ions and can trigger camera detection. Live feedback is enabled by the addition of a frame-grabber FPGA. The frame grabber receives real-time camera images through a Camera Link communication protocol, processes the images according to parameters uploaded via TCP/IP, and outputs the results in SPI form to the main FPGA. The latter is programmed to continue the sequence according to these results.

In order for this fast determination of the ion state to be employed for coherent feedback, it must be available for use in real time by the main FPGA controlling all other parts of the experiment. Therefore, some communication between the two is necessary. We realize one-way synchronous (clock-controlled) serial communication using a serial peripheral interface (SPI). The frame-grabber output is transferred to the main FPGA through the SPI, while the main FPGA is configured to wait for the measurement results and to incorporate conditioned operations based on these results. In the opposite direction, the main FPGA sends a trigger to both the camera and the frame grabber at the beginning of every experiment, preparing them for an upcoming measurement [48]. Our control scheme is shown diagrammatically in Fig. 8.

The speed with which the image is digitally read out by the camera, sent through Camera-Link to the frame grabber, processed, the results sent to the main FPGA, and the conditioned operation is triggered is orders of magnitude shorter than either the acquisition or readout time (over $500 \mu\text{s}$ each). Hence, this process introduces negligible time overhead.

The image-acquisition time, including both EMCCD exposure and readout time, is typically longer than 1 ms and can be as high as 2 ms, during which we require that the hidden ions maintain quantum coherence. However, the encoded states ($|0\rangle, |\bar{0}\rangle$) are highly susceptible to

magnetic fields and therefore magnetic noise in our laboratory limits the coherence times of the hidden qubits to about $500 \mu\text{s}$. This is strongly prohibitive for performing coherent feedback. In order to suppress noise, we apply dynamical decoupling (DD) pulses on the $4D_{5/2}$ manifold during the measurement of the rest of the qubits. The DD pulses are realized by driving an rf magnetic field resonant with the $4D_{5/2}$ Zeeman splitting. This produces a J_x Hamiltonian on the spin- $5/2$ Zeeman manifold and for a correct time exactly realizes an effective π pulse, translating the states $4D_{5/2,m} \leftrightarrow 4D_{5/2,-m}$. Thus, this operation flips magnetic susceptibility and can be used as an echo pulse to suppress noise. Moreover, this driving has no bearing on the 422-nm measurement, as either of the optical-qubit states remains within its Zeeman manifold. We realize the dynamical decoupling as a series of four echo pulses in a Carr-Purcell-Meiboom-Gill (CPMG) protocol [49,50].

A. Demonstrating coherent feedback

In order to verify and characterize the performance of the module, we perform two tests for which real-time coherent quantum feedback is necessary. Both experiments involve two qubits encoded on two ions: a control qubit, which is measured; and a target qubit, which is subject

to a feedback operation. For both experiments, the operation on the target qubit is successful only if it is correctly conditioned on the result of the measured qubit and if the target qubit remains coherent. For the first experiment, the two qubits are in a separable state, while in the second experiment, the ions are entangled prior to measurement.

In the first experiment, we prepare both qubits in the $|1\rangle$ state and apply a $\pi/2$ pulse, generating the separable state

$$|\psi_1\rangle = \frac{1}{2} (|11\rangle + i|10\rangle + i|01\rangle - |00\rangle). \quad (6)$$

We then hide the target qubit, measure the control qubit, and reverse the hiding process, according to the protocol described earlier. Finally, another $\pi/2$ pulse is applied on the target qubit, with a phase that is conditioned on the measurement result: $\phi - \pi/2$ if $|1\rangle$ is measured and $\phi + \pi/2$ if $|0\rangle$ is measured. As examples of the consequence of this conditioned operation, consider that in the case $\phi = \pi/2$, the target qubit will always be found in the opposite state to that of the control, whereas in the case of $\phi = -\pi/2$, the target and control qubits will be measured in the same state. Note that if the operation is not conditioned on the measurement result, which is completely random, or if it is conditioned and the target qubit

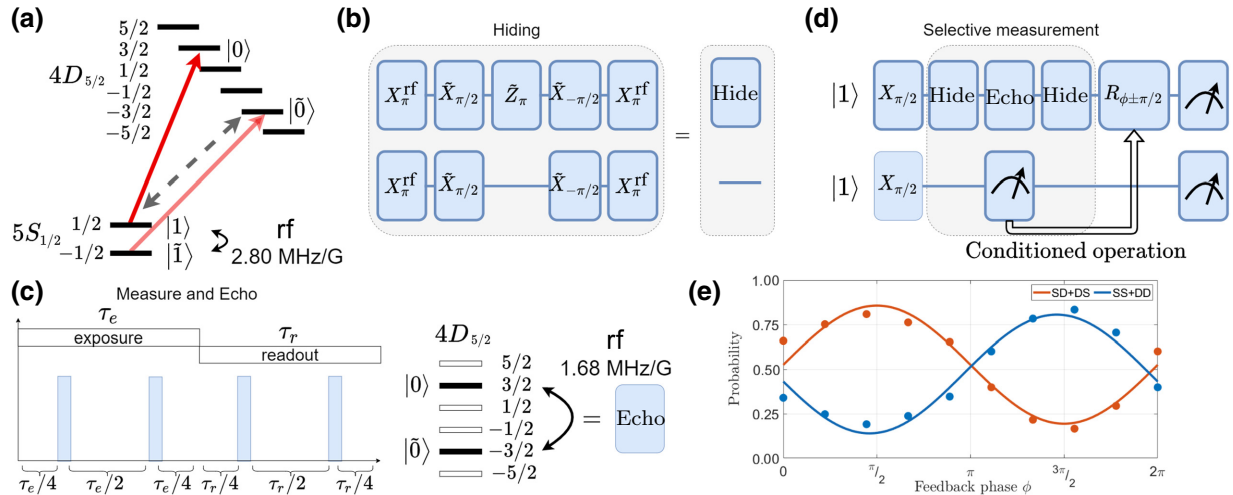


FIG. 9. (a) For qubits that should remain hidden from measurement, the $|1\rangle$ state is mapped onto $|\tilde{0}\rangle$; after the mapping procedure, these qubits are entirely encoded in the $4D_{5/2}$ manifold and are decoupled from the measurement process. (b) Mapping is carried out by a series of operations utilizing optical control of the standard optical qubit ($|0\rangle, |1\rangle$), a “shadow” optical qubit comprised of ($|\tilde{0}\rangle, |\tilde{1}\rangle$), and rf control of the $5S_{1/2}$ manifold qubit. Individual addressing pulses are used to single out the hidden ions. (c) After hiding, the remaining qubits are measured. During measurement, the hidden qubits must maintain coherence in the face of dephasing noise. We use rf pulses resonant with the D manifold Zeeman splitting to flip between $|0\rangle$ and $|\tilde{0}\rangle$, echoing out the noise. We apply four π pulses in a double CPMG configuration, such that noises during exposure and readout are decoupled separately. Typical times are $\tau_e \approx 700 \mu\text{s}$ and $\tau_r \approx 600 \mu\text{s}$. (d) In order to test coherent feedback, two qubits are initialized in the $|1\rangle$ state. We first apply a $\pi/2$ pulse on both qubits. Then, we apply a readout procedure, where one ion is hidden, the other is measured in parallel with the echo sequence shown in (c), and the hiding process is then reversed. Finally, a $\pi/2$ pulse is applied on the target qubit, with a phase that is controlled by the measurement result, and the two qubits are measured. (e) Parity-measurement results are plotted as a function of ϕ . For a nonconditioned pulse, or for total loss of coherence, we would expect a flat parity signal that is independent of phase. Instead, we measure an 0.83 success probability for the feedback operation, determined by the amplitude of the parity oscillations.

is no longer coherent, then the qubits will exhibit no correlations. More generally, we measure the correlation or anticorrelation of the control and target qubit-measurement outcomes as a function of ϕ . We successfully realize our desired correlation with a probability of 0.832(24), compared to random 0.5 probability, as shown in Fig. 9(e). The main source of error is likely the remaining magnetic field noise, along with imperfect implementation of DD rf pulses leading to population remaining in the $4D_{5/2}$ manifold.

In a second experiment, we prepare the two qubits in the maximally entangled Bell state $|\psi_{\text{Bell}}\rangle = 1/\sqrt{2}(|11\rangle + i|00\rangle)$ using the MS gate. This is followed by a $\pi/2$ pulse on the control qubit, leading to the state

$$|\psi'_{\text{Bell}}\rangle = \frac{1}{\sqrt{2}}(|\tilde{+}\rangle + i|\tilde{-}\rangle), \quad (7)$$

where $|\tilde{\pm}\rangle = 1/\sqrt{2}(|1\rangle \pm i|0\rangle)$ are Pauli Y eigenstates. We then hide the target qubit, measure the control qubit, and reverse the hiding of the target qubit, with a sequence identical to that described above.

The measurement projects the two-qubit state to either $|1\rangle \otimes [1/\sqrt{2}(|1\rangle + i|0\rangle)] = |1\tilde{+}\rangle$ or $|0\rangle \otimes [1/\sqrt{2}(|1\rangle - i|0\rangle)] = |0\tilde{-}\rangle$. The target qubit is therefore projected onto a superposition state with some well-defined phase, which is exactly opposite for the two cases. Finally, as in the previous experiment, we apply a $\pi/2$ pulse with phase $\phi - \pi/2$ if the control is measured as $|1\rangle$ and $\phi + \pi/2$ if the control is measured as $|0\rangle$. For conditioned coherent experiments, $\phi = \pi/2$ should always generate $|0\rangle$ on the target qubit, while $\phi = 3\pi/2$ should always generate $|1\rangle$. The measurement result is completely random but because we exploit the correlation between the entangled

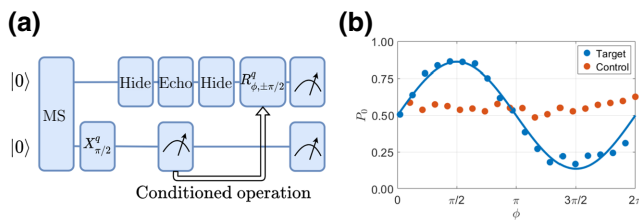


FIG. 10. Coherent feedback on an entangled state. (a) A two-qubit maximally entangled Bell state is prepared using an MS gate, followed by a $\pi/2$ pulse on the control qubit. Then, the target qubit is hidden, a measurement is performed along with echo pulses, and the target qubit is mapped back onto the optical qubit. A $\pi/2$ pulse with a phase $\phi - \pi/2$ or $\phi + \pi/2$ is applied conditioned on the measurement result. (b) The qubit population as a function of ϕ . Due to the initial entanglement, the measurement collapses the target qubit onto a superposition state defined by the control-qubit measurement result. This phase is effectively measured by applying the $\pi/2$ pulse. We measure an 0.862(18) success probability.

qubits, the conditioned operation results in a deterministic outcome. Moreover, correct feedback relies on the phase coherence of the target qubit. For this measurement, we report a success probability of 0.863(15), on a par with the previous experiment, as can be seen in Fig. 10.

While we demonstrate all the necessary ingredients for performing quantum error correction with our system, our coherent feedback fidelities need to be improved. The main source of error is decoherence due to magnetic noise during the readout time of the EMCCD camera, which is lower limited by an overhead of approximately 300 μs . Future systems, incorporating magnetic shielding and stabilization and possibly the use of faster detectors, will potentially increase fidelity.

VI. CONCLUSIONS

Trapped ions are among the leading candidate technologies for the realization of a large-scale quantum computer. Such a large-scale quantum computer is likely to be composed out of an interconnected network of smaller high-quality quantum registers.

Here, we describe and characterize a small-scale five-qubit quantum register and introduce two important features. The first is the implementation of two-qubit gates that are robust against gate timing errors. Gates executed on pairs of ion qubits out of a longer chain are more prone to errors than when executed on two-ion crystals. The use of robust gates is therefore important in order to reach high-fidelity gates in longer crystals. The second feature is our demonstration of midcircuit measurement and coherent feedback using a camera. The ability to perform midcircuit measurement and feedback is at the heart of most quantum error-correction schemes and other protocols such as entanglement distillation and quantum teleportation, all of which are likely to be important ingredients in large-scale quantum computing. The use of a camera for realizing such capabilities presents an inherently scalable path for larger future experiments. Furthermore, the presented scheme for camera-based coherent feedback can be straightforwardly adapted to neutral-atom quantum processors, which typically use similar CCD cameras and detection techniques [51–53].

ACKNOWLEDGMENTS

This work was performed with the support of the Israeli Science Foundation. The Willner Family Leadership Institute for the Weizmann Institute of Science, The Crown Photonics Center, and the Rosa and Emilio Segre Research Award.

- [1] R. Ozeri, The trapped-ion qubit tool box, *Contemp. Phys.* **52**, 531 (2011).

- [2] D. Kielpinski, C. Monroe, and D. J. Wineland, Architecture for a large-scale ion-trap quantum computer, *Nature* **417**, 709 (2002).
- [3] Y. Wan, D. Kienzler, S. D. Erickson, K. H. Mayer, T. R. Tan, J. J. Wu, H. M. Vasconcelos, S. Glancy, E. Knill, D. J. Wineland, A. C. Wilson, and D. Leibfried, Quantum gate teleportation between separated qubits in a trapped-ion processor, *Science* **364**, 875 (2019).
- [4] J. M. Pino, J. M. Dreiling, C. Figgatt, J. P. Gaebler, S. A. Moses, M. S. Allman, C. H. Baldwin, M. Foss-Feig, D. Hayes, and K. Mayer *et al.*, Demonstration of the trapped-ion quantum ccd computer architecture, *Nature* **592**, 209 (2021).
- [5] C. Monroe, R. Raussendorf, A. Ruthven, K. R. Brown, P. Maunz, L.-M. Duan, and J. Kim, Large-scale modular quantum-computer architecture with atomic memory and photonic interconnects, *Phys. Rev. A* **89**, 022317 (2014).
- [6] D. Hucul, I. V. Inlek, G. Vittorini, C. Crocker, S. Debnath, S. M. Clark, and C. Monroe, Modular entanglement of atomic qubits using photons and phonons, *Nat. Phys.* **11**, 37 (2015).
- [7] N. M. Linke, D. Maslov, M. Roetteler, S. Debnath, C. Figgatt, K. A. Landsman, K. Wright, and C. Monroe, Experimental comparison of two quantum computing architectures, *Proc. Natl. Acad. Sci.* **114**, 3305 (2017).
- [8] J. Chiaverini, D. Leibfried, T. Schaetz, M. D. Barrett, R. Blakestad, J. Britton, W. M. Itano, J. D. Jost, E. Knill, and C. Langer *et al.*, Realization of quantum error correction, *Nature* **432**, 602 (2004).
- [9] P. Schindler, J. T. Barreiro, T. Monz, V. Nebendahl, D. Nigg, M. Chwalla, M. Hennrich, and R. Blatt, Experimental repetitive quantum error correction, *Science* **332**, 1059 (2011).
- [10] V. Negnevitsky, M. Marinelli, K. K. Mehta, H.-Y. Lo, C. Flühmann, and J. P. Home, Repeated multi-qubit readout and feedback with a mixed-species trapped-ion register, *Nature* **563**, 527 (2018).
- [11] R. Stricker, D. Vodola, A. Erhard, L. Postler, M. Meth, M. Ringbauer, P. Schindler, T. Monz, M. Müller, and R. Blatt, Experimental deterministic correction of qubit loss, *Nature* **585**, 207 (2020).
- [12] C. Ryan-Anderson, J. Bohnet, K. Lee, D. Gresh, A. Hankin, J. Gaebler, D. Francois, A. Chernoguzov, D. Lucchetti, and N. Brown *et al.*, Realization of Real-Time Fault-Tolerant Quantum Error Correction, *Phys. Rev. X* **11**, 041058 (2021).
- [13] A. Erhard, H. Poulsen Nautrup, M. Meth, L. Postler, R. Stricker, M. Stadler, V. Negnevitsky, M. Ringbauer, P. Schindler, and H. J. Briegel *et al.*, Entangling logical qubits with lattice surgery, *Nature* **589**, 220 (2021).
- [14] D. Zhu, G. D. Kahanamoku-Meyer, L. Lewis, C. Noel, O. Katz, B. Harraz, Q. Wang, A. Risinger, L. Feng, and D. Biswas *et al.*, Interactive protocols for classically-verifiable quantum advantage, arXiv preprint [arXiv:2112.05156](https://arxiv.org/abs/2112.05156) (2021).
- [15] P. Schindler, D. Nigg, T. Monz, J. T. Barreiro, E. Martinez, S. X. Wang, S. Quint, M. F. Brandl, V. Nebendahl, and C. F. Roos *et al.*, A quantum information processor with trapped ions, *New J. Phys.* **15**, 123012 (2013).
- [16] I. Pogorelov, T. Feldker, C. D. Marciniak, L. Postler, G. Jacob, O. Kriegelsteiner, V. Podlesnic, M. Meth, V. Negnevitsky, M. Stadler, B. Höfer, C. Wächter, K. Lakhmanskiy, R. Blatt, P. Schindler, and T. Monz, Compact ion-trap quantum computing demonstrator, *PRX Quantum* **2**, 020343 (2021).
- [17] S. Debnath, N. M. Linke, C. Figgatt, K. A. Landsman, K. Wright, and C. Monroe, Demonstration of a small programmable quantum computer with atomic qubits, *Nature* **536**, 63 (2016).
- [18] K. Wright *et al.*, Benchmarking an 11-qubit quantum computer, *Nat. Commun.* **10**, 5464 (2019).
- [19] Y. Lu, S. Zhang, K. Zhang, W. Chen, Y. Shen, J. Zhang, J.-N. Zhang, and K. Kim, Global entangling gates on arbitrary ion qubits, *Nature* **572**, 363 (2019).
- [20] J. P. Home, D. Hanneke, J. D. Jost, J. M. Amini, D. Leibfried, and D. J. Wineland, Complete methods set for scalable ion trap quantum information processing, *Science* **325**, 1227 (2009).
- [21] J. M. Pino, J. M. Dreiling, C. Figgatt, J. P. Gaebler, S. A. Moses, M. S. Allman, C. H. Baldwin, M. Foss-Feig, D. Hayes, K. Mayer, C. Ryan-Anderson, and B. Neyenhuis, Demonstration of the trapped-ion quantum ccd computer architecture, *Nature* **592**, 209 (2021).
- [22] J. Hilder, D. Pijn, O. Onishchenko, A. Stahl, M. Orth, B. Lekitsch, A. Rodriguez-Blanco, M. Müller, F. Schmidt-Kaler, and U. Poschinger, Fault-tolerant parity readout on a shuttling-based trapped-ion quantum computer, arXiv preprint [arXiv:2107.06368](https://arxiv.org/abs/2107.06368) (2021).
- [23] Y. Shapira, R. Shaniv, T. Manovitz, N. Akerman, and R. Ozeri, Robust Entanglement Gates for Trapped-Ion Qubits, *Phys. Rev. Lett.* **121**, 180502 (2018).
- [24] A. E. Webb, S. C. Webster, S. Collingbourne, D. Breaud, A. M. Lawrence, S. Weidt, F. Mintert, and W. K. Hensinger, Resilient Entangling Gates for Trapped Ions, *Phys. Rev. Lett.* **121**, 180501 (2018).
- [25] G. Zarantonello, H. Hahn, J. Morgner, M. Schulte, A. Bautista-Salvador, R. Werner, K. Hammerer, and C. Ospelkaus, Robust and Resource-Efficient Microwave Near-Field Entangling ${}^9\text{Be}^+$ Gate, *Phys. Rev. Lett.* **123**, 260503 (2019).
- [26] T. Manovitz, A. Rotem, R. Shaniv, I. Cohen, Y. Shapira, N. Akerman, A. Retzker, and R. Ozeri, Fast Dynamical Decoupling of the Mølmer-Sørensen Entangling Gate, *Phys. Rev. Lett.* **119**, 220505 (2017).
- [27] N. Akerman, Y. Glickman, S. Kotler, A. Keselman, and R. Ozeri, Quantum control of ${}^{88}\text{Sr}^+$ in a miniature linear Paul trap, *Appl. Phys. B* **107**, 1167 (2011).
- [28] N. Akerman, Ph.D. thesis, Weizmann Institute of Science, Feinberg Graduate School, 2012.
- [29] L. Peleg, N. Akerman, T. Manovitz, M. Alon, and R. Ozeri, Phase stability transfer across the optical domain using a commercial optical frequency comb system, arXiv preprint [arXiv:1905.05065](https://arxiv.org/abs/1905.05065) (2019).
- [30] R. Lechner, C. Maier, C. Hempel, P. Jurcevic, B. P. Lanyon, T. Monz, M. Brownnutt, R. Blatt, and C. F. Roos, Electromagnetically-induced-transparency ground-state cooling of long ion strings, *Phys. Rev. A* **93**, 053401 (2016).
- [31] D. F. James, Quantum dynamics of cold trapped ions with application to quantum computation, Quantum Computation and Quantum Information Theory: Reprint Volume with Introductory Notes for ISI TMR Network School,

- 12–23 July 1999, Villa Gualino, Torino, Italy **66**, 345 (2000).
- [32] I. Pogorelov, T. Feldker, C. D. Marciniak, L. Postler, G. Jacob, O. Kriegelsteiner, V. Podlesnic, M. Meth, V. Negnevitsky, and M. Stadler *et al.*, Compact ion-trap quantum computing demonstrator, *PRX Quantum* **2**, 020343 (2021).
- [33] F. Mintert and C. Wunderlich, Ion-Trap Quantum Logic Using Long-Wavelength Radiation, *Phys. Rev. Lett.* **87**, 257904 (2001).
- [34] M. Johanning, A. Braun, N. Timoney, V. Elman, W. Neuhauser, and C. Wunderlich, Individual Addressing of Trapped Ions and Coupling of Motional and Spin States Using rf Radiation, *Phys. Rev. Lett.* **102**, 073004 (2009).
- [35] N. Timoney, I. Baumgart, M. Johanning, A. Varón, M. B. Plenio, A. Retzker, and C. Wunderlich, Quantum gates and memory using microwave-dressed states, *Nature* **476**, 185 (2011).
- [36] N. Navon, S. Kotler, N. Akerman, Y. Glickman, I. Almog, and R. Ozeri, Addressing Two-Level Systems Variably Coupled to an Oscillating Field, *Phys. Rev. Lett.* **111**, 073001 (2013).
- [37] T. Manovitz, Master’s thesis, Weizmann Institute of Science, Feinberg Graduate School, 2016.
- [38] A. Sørensen and K. Mølmer, Quantum Computation with Ions in Thermal Motion, *Phys. Rev. Lett.* **82**, 1971 (1999).
- [39] A. Sørensen and K. Mølmer, Entanglement and quantum computation with ions in thermal motion, *Phys. Rev. A* **62**, 022311 (2000).
- [40] J. P. Gaebler, T. R. Tan, Y. Lin, Y. Wan, R. Bowler, A. C. Keith, S. Glancy, K. Coakley, E. Knill, and D. Leibfried *et al.*, High-Fidelity Universal Gate Set for ${}^9\text{Be}^+$ Ion Qubits, *Phys. Rev. Lett.* **117**, 060505 (2016).
- [41] C. Ballance, T. Harty, N. Linke, M. Sepiol, and D. Lucas, High-Fidelity Quantum Logic Gates Using Trapped-Ion Hyperfine Qubits, *Phys. Rev. Lett.* **117**, 060504 (2016).
- [42] R. Srinivas, S. Burd, H. Knaack, R. Sutherland, A. Kwiatkowski, S. Glancy, E. Knill, D. Wineland, D. Leibfried, and A. Wilson *et al.*, High-fidelity laser-free universal control of two trapped ion qubits, arXiv preprint [arXiv:2102.12533](https://arxiv.org/abs/2102.12533) (2021).
- [43] C. R. Clark, H. N. Tinkey, B. C. Sawyer, A. M. Meier, K. A. Burkhardt, C. M. Seck, C. M. Shappert, N. D. Guise, C. E. Volin, and S. D. Fallek *et al.*, High-fidelity Bell-state preparation with ${}^{40}\text{Ca}^+$ optical qubits, arXiv preprint [arXiv:2105.05828](https://arxiv.org/abs/2105.05828) (2021).
- [44] Y. Shapira, R. Shaniv, T. Manovitz, N. Akerman, L. Peleg, L. Gazit, R. Ozeri, and A. Stern, Theory of robust multi-qubit nonadiabatic gates for trapped ions, *Phys. Rev. A* **101**, 032330 (2020).
- [45] C. Figgatt, A. Ostrander, N. M. Linke, K. A. Landsman, D. Zhu, D. Maslov, and C. Monroe, Parallel entangling operations on a universal ion-trap quantum computer, *Nature* **572**, 368 (2019).
- [46] D. Aharonov and M. Ben-Or, in *Proceedings of the twenty-ninth annual ACM symposium on Theory of computing* (1997), p. 176.
- [47] E. Knill and R. Laflamme, Theory of quantum error-correcting codes, *Phys. Rev. A* **55**, 900 (1997).
- [48] L. Gazit, Master’s thesis, Weizmann Institute of Science, Feinberg Graduate School, 2020.
- [49] H. Y. Carr and E. M. Purcell, Effects of diffusion on free precession in nuclear magnetic resonance experiments, *Phys. Rev.* **94**, 630 (1954).
- [50] S. Meiboom and D. Gill, Modified spin-echo method for measuring nuclear relaxation times, *Rev. Sci. Instrum.* **29**, 688 (1958).
- [51] M. Norcia, A. Young, and A. Kaufman, Microscopic Control and Detection of Ultracold Strontium in Optical-Tweezer Arrays, *Phys. Rev. X* **8**, 041054 (2018).
- [52] S. Ebadi, T. T. Wang, H. Levine, A. Keesling, G. Semeghini, A. Omran, D. Bluvstein, R. Samajdar, H. Pichler, and W. W. Ho *et al.*, Quantum phases of matter on a 256-atom programmable quantum simulator, *Nature* **595**, 227 (2021).
- [53] D. Bluvstein, H. Levine, G. Semeghini, T. T. Wang, S. Ebadi, M. Kalinowski, A. Keesling, N. Maskara, H. Pichler, and M. Greiner *et al.*, A quantum processor based on coherent transport of entangled atom arrays, arXiv preprint [arXiv:2112.03923](https://arxiv.org/abs/2112.03923) (2021).